Journal of
Micro/Nanolithography,
MEMS, and MOEMS

Nanolithography.SPIEDigitalLibrary.org

Reconstructing the three-dimensional latent image of extreme ultraviolet resists with resonant soft x-ray scattering

Guillaume Freychet
Isvar A. Cordova
Terry McAfee
Dinesh Kumar
Ronald J. Pandolfi
Chris Anderson
Scott D. Dhuey
Patrick Naulleau
Cheng Wang
Alexander Hexemer

SPIE.

Guillaume Freychet, Isvar A. Cordova, Terry McAfee, Dinesh Kumar, Ronald J. Pandolfi, Chris Anderson, Scott D. Dhuey, Patrick Naulleau, Cheng Wang, Alexander Hexemer, "Reconstructing the three-dimensional latent image of extreme ultraviolet resists with resonant soft x-ray scattering," *J. Micro/Nanolith. MEMS MOEMS* **18**(2), 024003 (2019), doi: 10.1117/1.JMM.18.2.024003.

Reconstructing the three-dimensional latent image of extreme ultraviolet resists with resonant soft x-ray scattering

Guillaume Freychet,[a,*] Isvar A. Cordova,[a] Terry McAfee,[a,b] Dinesh Kumar,[a] Ronald J. Pandolfi,[a] Chris Anderson,[c] Scott D. Dhuey,[d] Patrick Naulleau,[c] Cheng Wang,[a] and Alexander Hexemer[a]
[a]Lawrence Berkeley National Laboratory, Berkeley, California, United States
[b]Washington State University, Pullman, Washington, United States
[c]Center for X-Ray Optics, Lawrence Berkeley National Laboratory, Berkeley, California, United States
[d]Molecular Foundry, Lawrence Berkeley National Laboratory, Berkeley, California, United States

Abstract. Extreme ultraviolet (EUV) lithography is one of the most promising printing techniques for high-volume semiconductor manufacturing at the 14-nm half-pitch device node and beyond. However, key challenges around EUV photoresist materials, such as the exposure-dose sensitivity or the line-width roughness, continue to impede its full adoption into industrial nanofab facilities. Metrology tools are required to address these challenges by helping to assess the impact of the EUV materials' properties and processing conditions along different steps of the nanofabrication process. We apply the resonant soft x-ray scattering (RSoXS) technique to gain insights into the structure of patterned EUV resists before the development step takes place. By using energies around the carbon K-edge to take advantage of small differences in chemistry, the electronic density contrast between the exposed and unexposed regions of the resists could be enhanced in order to image the patterns with subnanometer precision. Critical-dimension grazing-incidence small-angle x-ray scattering is then performed at energies where the contrast is maximized, enabling the reconstruction of the three-dimensional shape of the latent image. We demonstrate the potential of RSoXS to provide a high-resolution height-sensitive profile of patterned EUV resists, which will help in quantifying the evolution of critical features, such as the line-edge roughness, at a key step of the nanofabrication process.
[DOI: 10.1117/1.JMM.18.2.024003]

Keywords: x-ray scattering; resonant soft x-ray scattering; extreme ultraviolet lithography; latent image; critical-dimension grazing-incidence small-angle x-ray scattering; near-edge x-ray absorption fine structure.

Paper 18149 received Dec. 20, 2018; accepted for publication Apr. 12, 2019; published online May 3, 2019.

1 Introduction

Lithographically manufactured nanostructures are shrinking in size in an effort to keep up with Moore's law. Extreme ultraviolet lithography (EUVL), with an imaging wavelength of 13.5 nm, is the next-generation lithography technology for high-volume manufacturing at the 14-nm half-pitch semiconductor device node and beyond.

The transition to EUVL not only brings challenges in terms of optics and mask design but also difficult metrology challenges. The continuous reduction in the size of semiconductor nanostructures has caused conventional techniques such as scanning electron microscopy and atomic force microscopy to start reaching their resolution limits.[1,2] Inline scatterometry techniques have been receiving increasing recognition for their potential to deliver solutions beyond these resolution limits and on industrially feasible timescales, as can be seen by their mention as an emerging disruptive metrology technology in the 2017 publication of the *International Roadmap for Devices and Systems* (*IRDS*).[3]

In particular, critical-dimension small-angle x-ray scattering (CD-SAXS) has emerged as one promising scatterometry technique to extract the profile of line gratings with subnanometer resolution.[4] CD-SAXS is a transmission-based scattering measurement where the sample is rotated in order to adjust the incident angle and extract the vertical profile. Sunday et al.[5,6] showed that such a measurement could be used to reconstruct the cross-sectional profile (i.e., width, height, and sidewall angle) of the line gratings as a stack of trapezoids. Since then, this approach has also been extended to the study of line-edge roughness.[7,8]

Moreover, Sunday et al.[9] also took advantage of the chemical sensitivity of resonant soft x-ray scattering (RSoXS) measurements to study diblock copolymer (PS-*b*-PMMA) gratings deposited on the ultrathin substrates with the transmission-based CD-SAXS approach. RSoXS leverages tunable "soft" x-ray (100 to 1500 eV) sources in order to dramatically enhance the scattering cross sections from heterogeneous materials when the x-ray photon energy is adjusted in order to coincide with a given material's x-ray absorption edges. This combination of absorption spectroscopy and scattering enhances the scattering contrast due to subtle differences in chemistry that are difficult to detect with conventional "hard" SAXS. In recent years, RSoXS performed near the carbon K-edge has proven to be a very useful tool for soft matter researchers interested in defining structure with subnanometer spatial sensitivity by leveraging small differences in chemistry.[10]

In this paper, we applied the RSoXS technique using energies around the carbon K-edge to enhance the effective

*Address all correspondence to Guillaume Freychet, E-mail: gfreychet@gmail.com

1932-5150/2019/$25.00 © 2019 SPIE

electronic density contrast due to chemical differences between the exposed and unexposed regions of a commercially available, chemically amplified EUV resist. Moreover, in contrast to conventional CD-SAXS, which has to be conducted in transmission geometry, this RSoXS measurement was performed in a reflection geometry on a standard Si wafer. This was only possible due to a recent advancement in the ability to confidently reconstruct three-dimensional (3-D) profiles from scattering data acquired in a grazing-incidence geometry (CD-GISAXS).[11–13] CD-GISAXS enabled the use of the low-energy, or soft, x-rays needed for the enhancement of scattering contrast due to chemical heterogeneities within the latent image (i.e., before the development step ever took place), while avoiding the need to penetrate a standard Si wafer. This capacity to nondestructively extract a statistically significant cross-sectional representation of the latent image from EUV resists deposited on a conventional Si wafer will provide invaluable feedback to the EUVL community in elucidating the impact of the development step on the final shape generated.

2 Experimental Section

2.1 *Sample Preparation*

Commercial chemically amplified EUV resists were studied in this paper. Throughout the process, minimal exposure to ambient or fluorescent light was ensured by storing samples in a completely dark sample holder and performing most of the necessary handling in a yellow-light class 100 cleanroom environment. The resist was spin-coated onto standard undoped Si wafers in order to yield a film roughly 45-nm thick, as illustrated in Fig. 1(a). Next, a post-application bake was conducted for 60 s at 130°C. The exposure of the resists was performed with a Vistec VB300 Electron Beam Lithography System using a dose of 133 $\mu C/cm^2$ to write a pattern over an area of 1 cm^2, as shown in Fig. 1(b). Finally, a post-exposure bake was conducted at 110°C for 60 s.

2.2 *6.3.2 Beamline*

Total electron yield near-edge x-ray absorption fine structure (TEY NEXAFS) spectra were collected at beamline 6.3.2 at the advanced light source (ALS).[14] Carbon K-edge spectra were obtained for the photon energy ranging from 270 to 400 eV. The data were normalized to the incident photon beam intensity measured by a photodiode.

2.3 *11.0.1.2 Beamline*

CD-GISAXS experiments were performed at beamline 11.0.1.2 at the ALS.[15] A CCD camera was positioned at 50 mm of the sample and the measurement were done at the carbon K-edge, i.e., between 250 and 300 eV. The line grating samples were aligned with a rotation stage until the incoming x-ray beam was parallel to the patterned lines, which was verified when a symmetric semicircle of Bragg spots appeared on the detector, as shown in Fig. 2(a). These Bragg spots will trace out linear features known as Bragg rods when the moment transfer vector is changed by either rotating the sample perpendicular to the substrate (i.e., along the z axis) or tilting the sample to different grazing angle of incidence (i.e., around the y axis). In our case, the angle of incidence range was set to tilt from 0.1 deg to 20 deg during each exposure in order to record the traces as Bragg rods covering the whole detector. Since the full width at half maximum diameter of the beam was 120 μm, the footprint of the beam on the sample will vary, respectively, between 70 and 300 μm. Since the beamstop's design was not optimized for this experiment and did not cover the whole CCD along the z axis, the detector was shifted in order to avoid saturation from the direct and specularly reflected beams. Therefore, as illustrated in Fig. 2(b), only half of the reciprocal space was probed. However, the missing part of the reciprocal space, illustrated in Fig. 2(a), was the symmetric analog of the collected data. The two-dimensional (2-D) image, shown in Fig. 2(b), was recorded with a 10-s acquisition time with the sample rotating at 0.3 revolutions per minute (rpm) during the acquisition.

3 Results and Discussion

3.1 *Near-Edge X-Ray Absorption Fine Structure*

The first step of the analysis is to determine whether there is any effective electronic density contrast induced in the EUV resist by the exposure step. To do so, we apply the near-edge x-ray absorption fine structure (NEXAFS) technique to record the imaginary part of the refractive index, β. Both 1×1 cm^2 fields of exposed and unexposed resists are measured at the ALS's beamline 6.3.2. The extracted β is shown in Fig. 3(a).

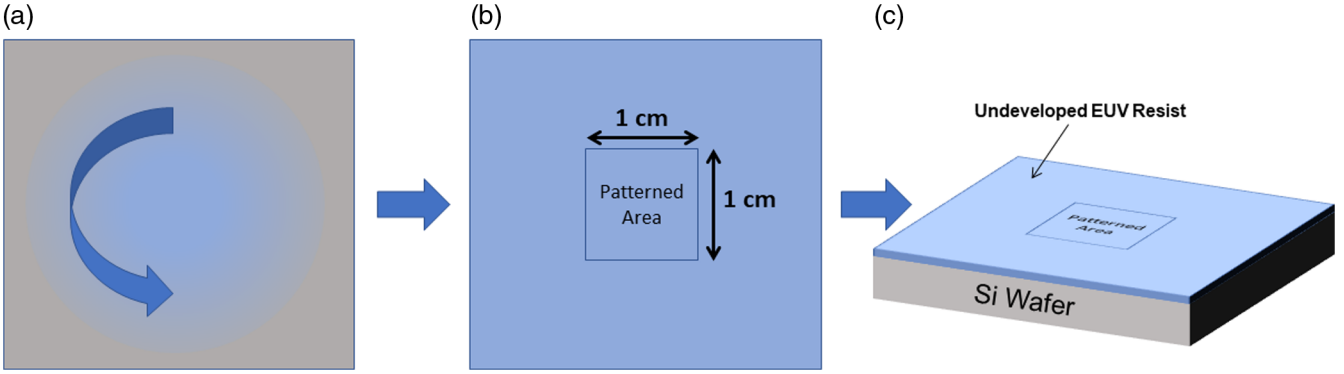

Fig. 1 Illustration of the sample (a) during the spin-coating step, (b) after the baking and exposure steps, and (c) during the GI-RSoXS measurement to extract the latent image.

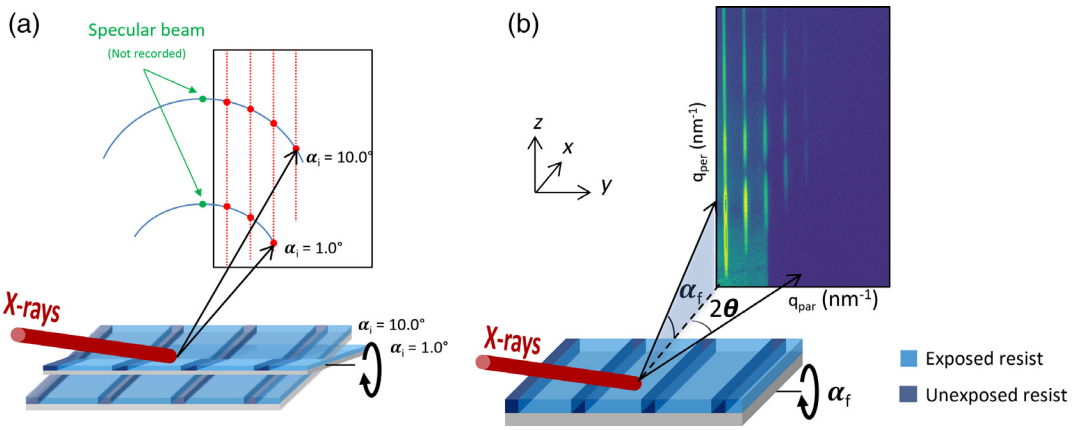

Fig. 2 Illustration of grazing-incidence small-angle x-ray scattering with the beam path oriented parallel to the *x*-axis and the sample tilting rotation around *y*-axis, (a) with constant incident angle of 1.0 deg and 10 deg and (b) with a continuous rotation of the sample from 0.1 deg to 20 deg.

From the imaginary component of the refractive index, the real component δ is calculated using the Kramers–Kronig relations.[16] Therefore, the full refractive index n can be calculated from measuring only the imaginary part

$$n = 1 - \delta + i\beta, \tag{1}$$

where δ is the dispersive component and β is the absorptive one. Both δ and β are shown on the Fig. 3(a).

The overall features of both δ and β are identical and only small variations can be observed between the two spectra. This leads to the conclusion that the chemical environment of the carbon atoms in the resist is not strongly modified by the EUV light exposure. However, the slight difference in intensity of the peaks observed at 288 and 295 eV, illustrated on the inset of Fig. 3(a), indicates a difference in the density of chemical states associated with that specific energy, which may correspond to the scission, or breaking, of specific carbon bonds in the resist that results from the EUV exposure and post-exposure bake steps.

For the RSoXS, the contrast between two chemical states with electronic density equal to ρ_1 and ρ_2 can be expressed as a sum of the square of the difference of δ and β

$$(\rho_2 - \rho_1)^2 = (\delta_2 - \delta_1)^2 + (\beta_2 - \beta_1)^2. \tag{2}$$

From both the delta and beta measured and calculated for the exposed and unexposed resists, we have calculated three different electronic density contrasts and plotted them in Fig. 3(c): between the exposed resist and vacuum (referred as Cev in the rest of the paper) (for which δ and β are equal to 0); between the unexposed resist and vacuum (referred as Cuv); and between the exposed resist and the unexposed resist (referred as Ceu). The similarity between both δ and β of the exposed and unexposed resists leads to a weak electronic density between resists. To better visualize this, a zoomed scale is presented in the inset of Fig. 3(c). More

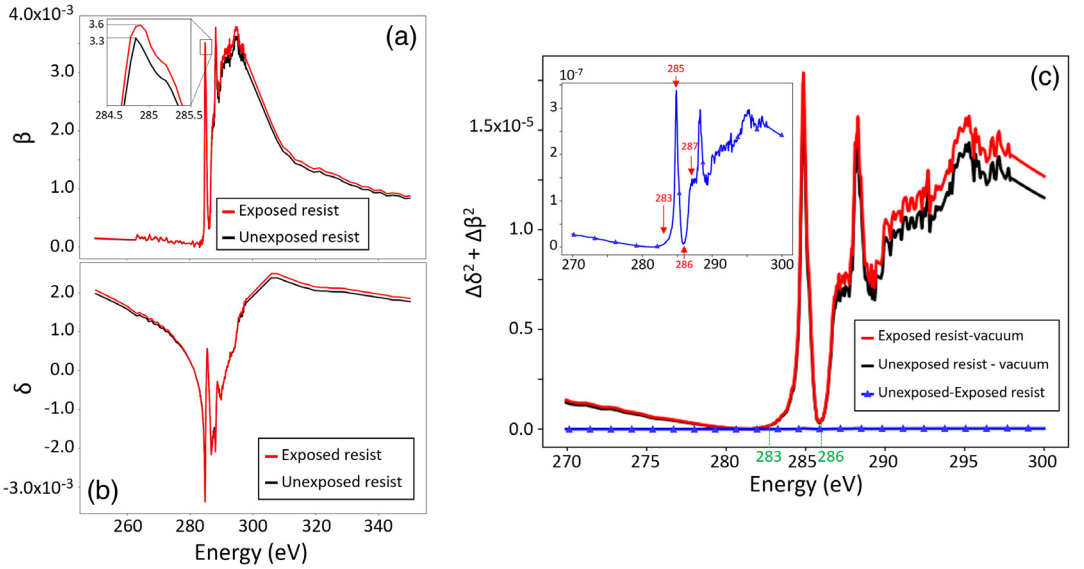

Fig. 3 (a) Real (δ) part with a inset zoomed around 285 eV and (b) imaginary (β) part of the complex indices of refraction of the exposed and unexposed resists, red and black lines respectively, and (c) the effective electronic density contrast ($\Delta\delta^2 + \Delta\beta^2$) between the two resists and the vacuum with scaled plot of the contrast between the two resists shown in the inset.

interestingly, for most energies, Ceu is negligible in comparison to Cev and Cuv, and except at specific energies around 280 and 287 eV, the three different electronic density contrasts have the same order of magnitude, making the relative contribution of Ceu to the observed scattering data more significant. Therefore, we have focused on collecting RSoXS measurements for the energy range from 280 to 290 eV.

3.2 *Resonant Soft X-Ray Scattering*

To record the Fourier rods, also known as Bragg rods, coming from the gratings, we scan the incident angle of the sample from 0.1 deg to 20 deg. We then decouple the various spatial contributions to the measured scattering features from the following expression of the q vector:

$$q = \begin{pmatrix} q_x \\ q_y \\ q_z \end{pmatrix} = \begin{pmatrix} \cos(\alpha_f)\cos(2\theta) - \cos(\alpha_i) \\ \cos(\alpha_f)\sin(2\theta) \\ \sin(\alpha_f) + \sin(\alpha_i) \end{pmatrix}, \tag{3}$$

where α_i, 2θ, and α_f represent the incident, in-plane, and out-of-plane scattering angles, respectively. Q-space will be decomposed as $q_{\text{par}} = \sqrt{q_x^2 + q_y^2}$ and $q_{\text{per}} = q_z$. Therefore, by scanning the incident angle (i.e., rotating the sample along the y axis) we scan the q_z direction of the reciprocal space. Representative 2-D images recorded at 283, 285, 286, and 287 eV are shown on Fig. 4 and are displayed in the pixel space, since each pixel will have a different coordinate in the q_{par} and q_{per} referential for each incident angle.

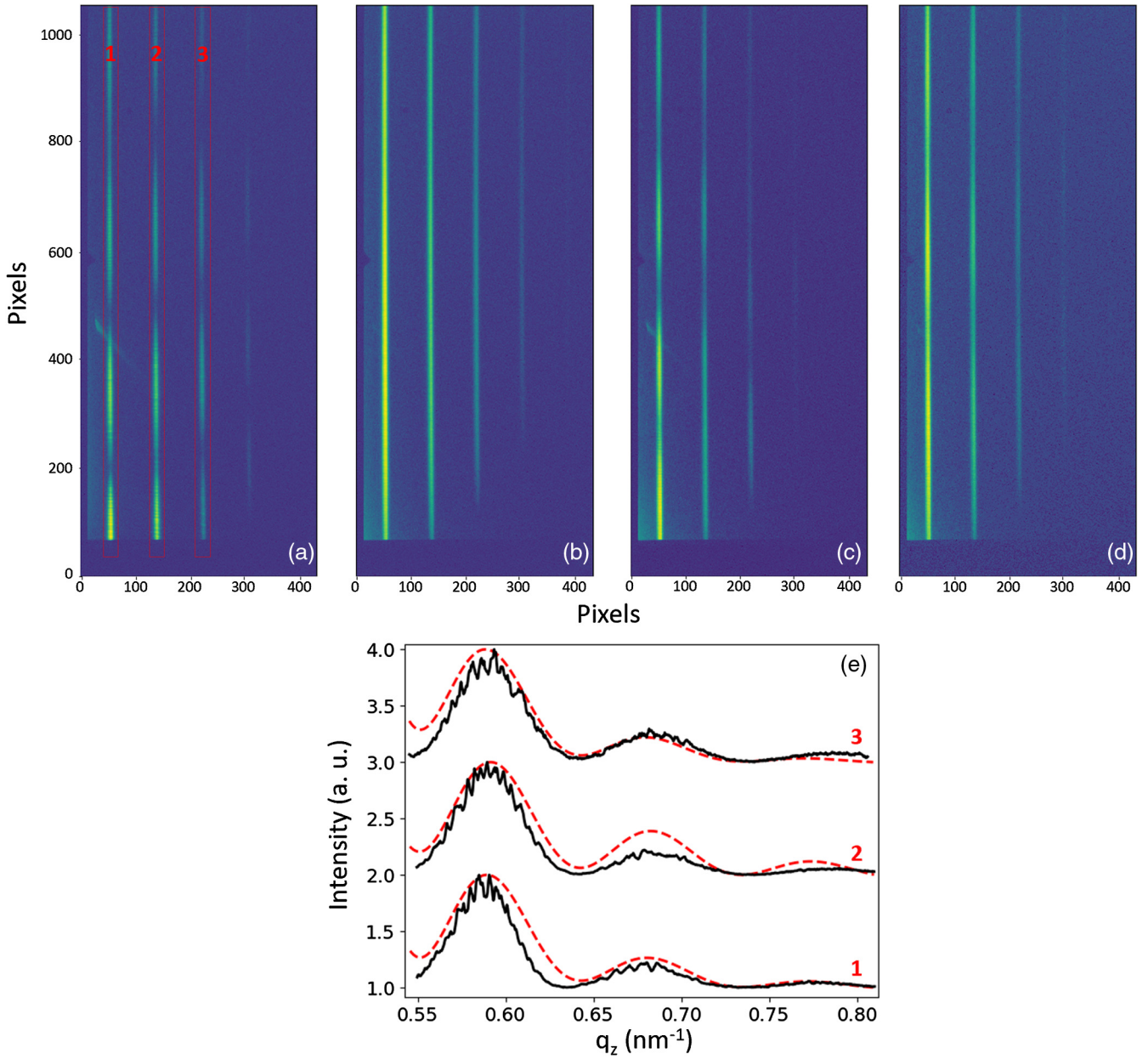

Fig. 4 The 2-D CD-GISAXS patterns recorded at (a) 283, (b) 285, (c) 286, and (d) 287 eV. (e) The 1-D plot of the averaged scattering intensity along the Bragg rods (black solid line) at 283 eV and the corresponding fit (red dashed lines).

The Bragg rods can be observed consistently across all four images, regardless of incident energy, confirming the presence of an in-plane structure inside the film. The presence of Bragg rods is unrelated to the presence of contrast between the exposed and unexposed resists. Indeed, in the hypothesis of any Cue equal to 0, the film of resist can be considered as a uniform film with a given height. In this scenario, the scattering signal will be concentrated at the specular plane, at $q_{par} = 0$ nm^{-1}. Therefore, only modulations of the reflected beam intensity would appear; however, our specific setup did not record this reciprocal space region. Not only does the presence of Bragg rods allow rejecting the assumption of an homogeneous film of resist, but it also reveals the existence of periodic features along the surface of the resist induced by the slight shrinking of the resist under EUV light, as illustrated in Fig. 5. Therefore, the $\Delta\ q_{par}$ distance between two consecutive Bragg rods can be used to extract the distance between two EUV exposures and therefore the pitch of the distance between two unexposed resist "lines." A value of 188.47 nm is extracted.

Figure 4 clearly shows that only some incident energies produce significant modulations along the lengths of the Bragg rods (i.e., q_{per}), while others do not. To illustrate this phenomenon, vertical one-dimensional cuts are done and are annotated in Fig. 4(a) taken at 283 eV. The first, second, and third Bragg rods are shown in Fig. 4(e).

Unlike the Bragg rods, the presence or absence of the modulations can be connected to the electronic density contrast calculated from the NEXAFS measurements. Our previous study on the CD-GISAXS method demonstrated that these modulations provide in-depth information on line gratings. This is because the intensity of the recorded Bragg rods is modulated by the Fourier transform of the shape of the individual lines.[17]

Consequently, the modulations at 283 and 286 eV reveal the existence of the electronic density contrast between the exposed and unexposed resists and are in agreement with a film thickness t_2 of 45 nm, as illustrated in Fig. 5. Conversely, the absence of modulations can be explained if there is no contrast between the resists. In that specific case, only a subnanometer height grating at the surface of the film is seen by the beam, coming from the shrinkage of the resist.

Therefore, we can only approximate from the intensity along the Bragg rods at 285 and 287 eV that the difference in thickness, t_1, between exposed and unexposed resists is <1 nm, as illustrated in Fig. 5. Such approximation is due to the fact that the first minimum of the form factor of such thin line should appear at $q_{per} > 5$ nm^{-1}, which is not accessible with the current instrumental setup (limited to $q_{per} < 2$ nm^{-1}).

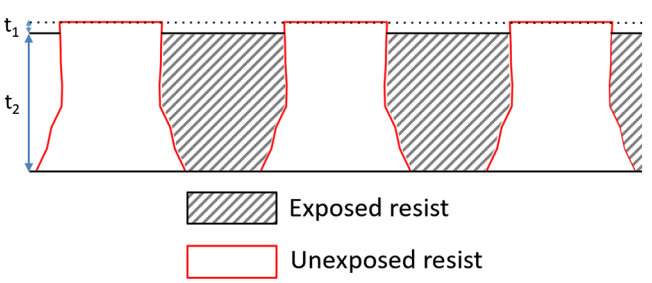

Fig. 5 Schematic representation of the in-depth profile of the latent image extracted with CD-GISAXS.

The electronic intensity contrast variation between resists observed with RSoXS follows the trend observed in the NEXAFS data. Indeed, the relative evolution of Cue with Cev and Cuv, leads to the same conclusions. Indeed, when Cue ~ Cev and Cuv, annotated with dash lines in Fig. 3(c), at 283 and 286 eV, for example, modulations along the Bragg rods can be observed. This differs starkly from the behavior at 285 and 287 eV, when Cue ≪ Cev and Cuv; no modulations along the Bragg rods are observed.

In addition, both height contributions to the form factor are weighted by Cue and Cuv. Therefore, at 283 and 286 eV, both form factors are visible on the Bragg rods, even though the form factor of the shallow gratings did not show any feature in that q-range. At 285 and 287 eV, since Cue ≪ Cev and Cuv, the form factor of the shallow gratings strongly dominates, even though some very weak modulations can be observed at 287 eV.

3.3 *In-Depth Profile Reconstruction*

To extract a detailed height profile of the latent image, the modulations along the Bragg rods at 283 eV are plotted in Fig. 4(e) and are fitted with an inverse algorithm. The height profile of the latent image can thus be described as a stack of trapezoids. The simulation of the form factor and subsequent reconstruction of the line shapes are done under the distorted-wave Born approximation (DWBA). The DWBA extends the Born approximation to include both reflective and refractive events at the film–substrate interface.[18,19]

The cross section of the depth profile of the latent image is approximated by stacking five trapezoids. The cross section can be described with $N + 2$ parameters, where N is the number of trapezoids and the parameters are each trapezoid's height, h (kept identical for all the trapezoids); a sidewall angle per trapezoid (assumed symmetric); and the bottom width of the trapezoid underneath.

To converge to the best cross-sectional profile of the line gratings, we used a genetic algorithm to minimize the difference between the form factor recorded experimentally and the simulated one.[11] Based on the study by Hannon et al.,[20] we applied a covariance matrix adaptation evolutionary strategy (CMAES).

The results of the CMAES are shown in Fig. 5, corresponding to the fit presented in Fig. 4(e). The best-fit profile comes from a stack of seven trapezoids, with each trapezoid having a height h of 6.23 nm, with an overall line-height of 43.60 nm, and a bottom linewidth of 87.20 nm. Each of the sidewall angles, from the bottom to the top are, respectively, equal to 71.8 deg, 81.7 deg, 71.5 deg, 88.9 deg, 92.5 deg, 90.7 deg, and 91.5 deg.

The fitted form factors show a good agreement with the experimental data; they mimic the position of the minima and the periodicity of the modulations. However, the amplitude is not perfectly reproduced. Our current simulation of a monodisperse line profile over the fully exposed area introduces some error in the reproduction of the modulation amplitude seen experimentally. Moreover, the possible depth variation of the electronic density contrast need also to be considered to improve the fit. A more detailed explanation on the simulation of the CD-GISAXS patterns recorded at different incident angles will be reported in a coming study

and a statistical distribution of the depth-profile model will be given.

The overall profiles also show the presence of a footing feature (i.e., a wider width at the bottom of the line at the substrate interface). However, no rounding effect at the top of the line can be observed. The next step of the study will be a comparison of the in-depth profile before and after the development of the exposed resist, in order to determine the significance and nature of both of these features.

4 Conclusion

In this study, we demonstrated the capability of the RSoXS technique to reconstruct the 3-D shape of the latent image in a EUV resist, before the development step took place.

The slight shrinkage of the resist under the EUV light, coupled with the chain scission of some carbon bonds, induced the appearance of a relatively weak electronic density contrast between the exposed and unexposed resists. Nevertheless, with a combination of NEXAFS and RSoXS measurements, we were able to enhance the effective electronic density contrast between the developed and undeveloped resists using energies around the carbon K-edge in order to detect the latent image on an EUV resist.

This study has given a first glimpse into the potential of the RSoXS technique to elucidate the structure of the exposed regions of the resists before development. Further studies using this approach are underway, such as quantifying the impact of the development step on the final profile and the impact of the soft x-rays, in order to provide insight to understand the physical and chemical phenomena underlying EUV lithography.

Acknowledgments

We acknowledge the support from the LBNL LDRD program, the DOE Early Career Award program, and the Center for Advanced Mathematics in Energy Research Applications (CAMERA), funded jointly through DOE's ASCR and BES programs. This work used resources of U.S. DOE Office of Science User Facilities, supported under contract Nos DE-SC0012704, DE-AC02-06CH11357, and DE-AC02-76SF00515. Work at the Molecular Foundry was supported by the Office of Science, Office of Basic Energy Sciences, of the U.S. Department of Energy under Contract No. DE-AC02-05CH11231. Terry McAfee was partially supported by NSF Grant No. 1626566.

References

1. R. Silver et al., "Fundamental limits of optical critical dimension metrology: a simulation study," *Proc. SPIE* **6518**, 65180U (2007).
2. B. Bunday et al., "Gaps analysis for CD metrology beyond the 22nm node," *Proc. SPIE* **8681**, 86813B (2013).
3. "International roadmap for devices and systems 2016," https://irds.ieee.org/.
4. T. Hu et al., "Small angle x-ray scattering metrology for sidewall angle and cross section of nanometer scale line gratings," *J. Appl. Phys.* **96**(4), 1983–1987 (2004).
5. D. F. Sunday et al., "Determining the shape and periodicity of nanostructures using small-angle x-ray scattering," *J. Appl. Crystallogr.* **48**, 1355–1363 (2015).
6. R. J. Pandolfi et al., "Xi-cam: a versatile interface for data visualization and analysis," *J. Synchrotron Radiat.* **25**, 1261–1270 (2018).
7. G. Freychet et al., "A study of lateral roughness evaluation through critical-dimension small angle x-ray scattering (CD-SAXS)," *Proc. SPIE* **9778**, 97783V (2016).
8. J. Reche et al., "Programmed line width roughness metrology by multitechniques approach," *J. Micro/Nanolithogr. MEMS MOEMS* **17**, 041005 (2018).
9. D. F. Sunday et al., "Determination of the internal morphology of nanostructures patterned by directed self assembly," *ACS Nano* **8**(8), 8426–8437 (2014).
10. C. Wang et al., "Defining the nanostructured morphology of triblock copolymers using resonant soft x-ray scattering," *Nano Lett.* **11**(9), 3906–3911 (2011).
11. G. Freychet et al., "Critical-dimension grazing incidence small angle x-ray scattering," *Proc. SPIE* **10585**, 1058512 (2018).
12. G. Freychet et al., "Estimation of line cross-sections in etched patterns using critical dimension grazing incidence small angle x-ray scattering," in preparation.
13. G. Freychet et al., "Using resonant soft x-ray scattering to image patterns on undeveloped resists," *Proc. SPIE* **10809**, 108090V (2018).
14. J. Underwood and E. Gullikson, "High-resolution, high-flux, user friendly VLS beamline at the ALS for the 50–1300ev energy region," *J. Electron. Spectrosc. Relat. Phenom.* **92**, 265–272 (1998).
15. E. Gann et al., "Soft x-ray scattering facility at the advanced light source with real-time data processing and analysis," *Rev. Sci. Instrum.* **83**(4), 045110 (2012).
16. B. Watts, "Calculation of the Kramers–Kronig transform of x-ray spectra by a piecewise Laurent polynomial method," *Opt. Express* **22**, 23628–23639 (2014).
17. G. Freychet et al., "Removal of poly(methyl methacrylate) in diblock copolymers films studied by grazing incidence small-angle x-ray scattering," *J. Polym. Sci. Part B Polym. Phys.* **54**(12), 1137–1144 (2016).
18. S. Sinha et al., "X-ray and neutron scattering from rough surfaces," *Phys. Rev. B* **38**(4), 2297–2311 (1988).
19. G. Renaud, R. Lazzari, and F. Leroy, "Probing surface and interface morphology with grazing incidence small angle x-ray scattering," *Surf. Sci. Rep.* **64**(8), 255–380 (2009).
20. A. F. Hannon et al., "Advancing x-ray scattering metrology using inverse genetic algorithms," *J. Micro/Nanolithogr. MEMS MOEMS* **15**, 034001 (2016).

Biographies of the authors are not available.